Ceramics International 51 (2025) 24903–24915

Contents lists available at ScienceDirect

Ceramics International

journal homepage: www.elsevier.com/locate/ceramint

Innovative defect engineering: A novel synthesis approach for an efficient Ti^{3+}-TiO_2/SiO_2 gas-phase-photocatalyst under UV–VIS radiation

Carolina Gusmão [a,*], Priscila Hasse Palharim [a], Bruno Ramos [a,b], Douglas Gouvêa [c], Orlando Rodrigues Júnior [d], Antonio Carlos Silva Costa Teixeira [a,**]

[a] Research Group in Advanced Oxidation Processes (AdOx), Department of Chemical Engineering, Escola Politécnica, University of São Paulo, São Paulo, SP, Brazil
[b] Microfluidic and Photoelectrocatalytic Engineering Lab (μFEC), Department of Chemical Engineering, Centro Universitario FEI, São Bernardo do Campo, SP, Brazil
[c] Laboratory of Ceramic Processes (LPC), Department of Material Engineering, Escola Politécnica, University of São Paulo, São Paulo, SP, Brazil
[d] Nuclear and Energy Research Institute, IPEN/CNEN, São Paulo, SP, Brazil

ARTICLE INFO

Handling Editor: Dr P. Vincenzini

Keywords:
Air treatment
Photocatalysis
Volatile organic compounds
Gas solid reactor
Crystal defects

ABSTRACT

Volatile Organic Compounds (VOCs) pose significant environmental and health risks, requiring the advancement of effective control techniques. This study presents a novel and cost-effective synthesis method for incorporating Ti^{3+} sites and oxygen vacancies into TiO_2 photocatalysts through sulfur doping, varying the thiourea content during synthesis. The synthesized modified TiO_2/SiO_2 materials were fully characterized using various techniques, including XRD, TEM, SEM, XPS, EPR, PL and BET. The analysis revealed the presence of crystalline defects. Notably, the EPR analysis indicated a correlation between the increase in bulk defects and the higher thiourea content. The photocatalytic efficiency of the synthesized materials was evaluated using *n*-hexane in a gas-solid reactor under UV–VIS radiation, showing a significant increase (34.2 % – 61.2 %) in degradation with the introduction of defects in the material. The operating conditions, such as humidity and the presence of oxygen, were varied, revealing a strong influence on the synthesized photocatalysts containing crystal defects. Notably, low humidity substantially increased photocatalytic activity, reaching 78.6 % degradation at 0 % of relative humidity. The stability of the material was examined over 180 min, with sustained high photocatalytic activity. Kinetic studies were carried out to explore varying input concentrations and transient regimes, providing valuable information on the performance of the continuous gas solid photocatalytic reactor (GSPR). This innovative synthesis approach is thus promising for efficient VOCs abatement with improved material performance and stability.

1. Introduction

Volatile organic compounds (VOCs), including aromatics, alcohols, ketones, alkanes and esters, present increased volatility, mobility, and resistance to degradation. Due to their serious threat to the environment and human health, various control techniques have been developed to remove VOCs [1–3]. Adsorption is a widely used recovery technique due to its efficiency, economy and potential to recover and reuse both the adsorbent and the contaminant [2,3]. Despite the high efficiency obtained with porous materials such as activated carbon, the high volume of waste produced is not attractive from an environmental and economical point of view. Thus, pollutant degradation technologies, such as the photocatalytic oxidation process (PCO), have stood out as effective methods due to their low cost, non-toxic nature, mild operational conditions, and resistance to photocorrosion [2,4].

In PCO, a semiconductor photocatalyst is exposed to light, generating highly reactive species that can convert pollutants into harmless substances. Amont the various photocatalysts used, TiO_2 is the most widely investigated due to its notable safety, stability, non-toxicity, abundance, relative low cost, and high photocatalytic activity [2,4]. However, it is known that low quantum efficiency in photocatalytic reactions, inefficient use of visible light due to high recombination rate of photoinduced electron-hole pairs, low mass transfer and a relatively large bandgap (~3.2 eV) are their main disadvantages. In order to adapt TiO_2 photocatalysts for VOC abatement it is essential to improve their catalytic properties. Researchers have tackled these challenges through

* Corresponding author.
** Corresponding author.
E-mail addresses: carolina.argusmao@gmail.com (C. Gusmão), acscteix@usp.br (A.C.S.C. Teixeira).

https://doi.org/10.1016/j.ceramint.2025.03.172
Received 23 May 2024; Received in revised form 18 February 2025; Accepted 11 March 2025
Available online 12 March 2025

various strategies, including supporting TiO_2 on materials with a higher specific surface area, doping with metal and non-metal ions, fabricating heterojunctions and composites, promoting surface sensitization by dyes, introducing defects and so on [5–7].

The introduction of defects in oxide semiconductors, such as Ti^{3+}, oxygen vacancies and lattice disorder defects, is a highly effective approach. Defects can alter the physical and chemical properties of catalytic materials, influencing the electronic energy levels, the local charge density, as well as the ability to adsorb and activate ions/molecules [7,8]. Xu et al. [5] introduced Ti^{3+} defects based on lattice distortion into TiO_2 microspheres, achieving a higher photocurrent and therefore an increase in photocatalytic activity of around three times under visible light irradiation. Zhang et al. [7] synthesized a series of Ti/TiO_2 materials by varying the interfacial Ti^{3+} sites using an epitaxial growth method under hydrothermal conditions. Because of the overlap and hybridization of various electronic orbitals, the Ti^{3+} sites could serve as visible-light responsive sites. Nevertheless, depending on the concentration of Ti^{3+} defects, they can also trap photogenerated electron-hole carriers, acting as recombination centers [7,9]. Thus, controlling the concentration of Ti^{3+} by different synthesis approaches, for example, is essential to achieve materials with improved performance.

Oxidation and reduction methods are the main approaches used to synthesize TiO_2 with Ti^{3+} sites. The reduction of Ti^{4+} to Ti^{3+} usually occurs concomitantly with oxygen loss on the TiO_2 surface, and can be accomplished under specific conditions, such as annealing under vacuum, heating under a reduction atmosphere or by electron beam. Reducing gases or lattice oxygen provide electrons to Ti^{4+} cations to form surface Ti^{3+} ions [10]. The oxidation of Ti^{2+} species into Ti^{3+}, in turn, can be achieved using simple techniques, such as solvothermal synthesis using TiH_2 in HCl solution, in which the Ti^{3+} concentration is adjusted by varying the synthesis temperature [11]. Another approach, namely the direct introduction of Ti^{3+}, relied on the introduction of Ti^{3+} ions into TiO_2 directly from the $TiCl_3$ precursor, for example. Zhu et al. [12] used $TiCl_3$ and TiF_4 as precursors and ethanol as a solvent to directly introduce Ti^{3+} by solvothermal synthesis. In this method, TiF_4, the source of Ti^{4+}, was added to the system to prevent the oxidation of Ti^{3+} during the reaction. Likewise, ion doping can also be used to introduce impurity atoms, such as F, N or S, into TiO_2, partially altering the concentration of electrons because of the difference in electronegativity [13].

In this work, we developed an innovative and low-cost synthesis approach to introduce Ti^{3+} sites and oxygen vacancies into TiO_2 photocatalysts through sulfur doping of the material, varying the thiourea content added in the synthesis. The samples were supported on silica to allow the formation of the bed in a continuous flow reactor for VOC abatement. In addition, the use of SiO_2 as a support increases the exposure of the nano-TiO_2 to irradiation, because in a continuous gas-solid reactor, the TiO_2 nanoparticles would agglomerate, requiring a much larger mass of the semiconductor, which would increase the costs of the photocatalytic process. Finally, previous studies [16,17] have shown that the use of silica as a support for TiO_2 in the proportions established in this work also contributes to the generation of Ti^{3+} and oxygen vacancies. The materials were characterized by XRD, TEM, SEM, XPS, EPR, PL and BET techniques. The photocatalytic activity of the materials was evaluated through experimental tests in a continuous fixed-bed reactor, using *n*-hexane as a model contaminant in the gas phase under UV–VIS irradiation, considering the inlet and outlet concentrations of the organic compound in the reactor. Photocatalytic tests were also carried out by varying the operating conditions, such as the relative humidity of the gas stream and the presence of oxygen, to assess the effect of these parameters on the photocatalytic reaction. Finally, the stability of the material that exhibited the greatest photocatalytic activity was evaluated by means of a prolonged 180-min assay with *n*-hexane degradation, and a kinetic study was conducted by varying the inlet concentrations and transient regimes in the continuous fixed-bed reactor.

2. Materials and methods

2.1. Materials

Titanium isopropoxide IV (TTiP, 97 %), silica-gel 63–200 μm and thiourea (>99 %) were purchased from Sigma-Aldrich. Nitric acid (HNO_3, 65 %) and *n*-hexane (C_6H_{14}, 96 %) were supplied by Merck. These chemicals were used without further purification. Ultrapure water (18.2 MΩ cm) from a Milli-Q® system was used to prepare all the solutions.

2.2. Photocatalyst synthesis

The coating of silica gel (specific surface area SiO_2, 300 $m^2\ g^{-1}$) with TiO_2 nanocrystals was carried out using the acid sol-gel method described in Chen et al. [14]. Subsequently, the synthesis of S-doped TiO_2/SiO_2 was adapted from the method described by Gusmão et al. [15]. The TiO_2/SiO_2 and S-TiO_2/SiO_2 samples were synthesized with four different sulfur contents. The mass of the sulfur precursor added to the samples are shown in Table 1.

First, a certain amount, defined in Table 1, of thiourea was added to 100 mL of ethanol (>99.5 %) in a thermostatic bath at 50 °C. 60 min later, 8.4 mL of TTIP was slowly added to this solution under vigorous and continuous stirring. Subsequently, 20 mL of Milli-Q® water was poured into the sol formed and the pH was reduced to 2.0 by with the addition of a 1 mol L^{-1} HNO_3 solution. After 60 min, 9.0 g of silica gel was mixed into the gel formed. The pH was then increased to 3.0 with the addition of a 1 mol L^{-1} NaOH solution. Finally, the gel was placed in dialysis membrane tubes and immersed in a Milli-Q® water bath for 96 h in order to increase the supernatant pH to 6 through ion exchange. Lastly, the gel was dried at 80 °C for 48 h and then calcined at 450 °C for 240 min in room atmosphere (heating ramp = 5 °C min^{-1}). After calcination, the synthesized materials were sieved in a diameter range of 75–180 μm.

2.3. Characterization techniques

The investigation of catalyst particle size and morphology involved various analytical techniques. Scanning electron microscopy (SEM-FESEM JSM-7401F JEOL) coupled with energy dispersive spectroscopy (EDS) (Thermo scientific NSS spectral imaging) was utilized to examine particle morphology and obtain a qualitative estimate of element distribution. High resolution transmission electron microscopy (HRTEM) images were obtained with a TEM JEOL JEM-2100 instrument. To prepare the samples for analysis, S_TiO_2/SiO_2 particles were dispersed in ethanol and subjected to an ultrasonic bath for 30 min. A small droplet of the sample solution was then pipetted onto a carbon grid. Finally, the solvent was evaporated, leaving behind the powder particles on the grid.

Information on the crystal structure, including the crystalline phases, crystal size, lattice parameters, and microstrain, was acquired by means of X-ray diffraction in the 2θ range of 20–80° at a scan rate of 0.02° s^{-1} (D8 Focus - Bruker AXS, Cu-Kα - 0.154 nm). The light absorption properties of the catalyst were determined through diffuse reflectance spectroscopy (DRS) using a UV 2550 (Shimadzu), and the surface area was measured using the Brunauer-Emmett-Teller (BET) method (Micrometrics Gemini III 2375).

The effective sulfur content of the S_TiO_2/SiO_2 materials was assessed using energy dispersive X-ray spectroscopy (EDX) (NEX-RIGAKU). X-ray photoelectron spectroscopy (XPS) (Thermo Scientific, K-Alpha, Al Kα 1486.6 eV, X-ray spot size of 400 μm, 10-8 mBar) was used to evaluate the energy states of the elements on the photocatalytic surface. For this analysis, 5 mg of the catalysts were affixed to an aluminium strip and degassed in an ultra-high vacuum (UHV) chamber at 25 °C.

Table 1
Synthesis conditions and characterization results of all synthesized photocatalyst samples.

Sample	Theoretical sulfur/TiO_2 weight ratio	Effective sulfur/TiO_2 weight ratio	Specific surface area ($m^2\ g^{-1}$)	Crystal size (nm)	E_g (eV)	E_{VB} (eV)	E_{CB} (eV)
TiO_2/SiO_2	–	–	404.2	4.3 ± 0.1	3.19	2.93	−0.25
1_S_TiO_2/SIO_2	0.9	0.013	394.7	5.1 ± 0.1	3.07	2.87	−0.19
2_S_TiO_2/SIO_2	1.8	0.015	375.5	5.3 ± 0.1	3.04	2.86	−0.17
3_S_TiO_2/SIO_2	3.6	0.023	354.1	5.5 ± 0.1	3.04	2.86	−0.17
4_S_TiO_2/SIO_2	5.0	0.025	328.3	5.8 ± 0.1	3.11	2.90	−0.21

Electron paramagnetic resonance spectroscopy (EPR) was used to analyse TiO_2/SiO_2, 2_S_TiO_2/SiO_2 and 4_S_TiO_2/SiO_2 materials. Finally, the photoluminescence spectra were determined at room temperature using a Fluorolog-3 fluorospectrophotometer equipped with a Xe lamp for excitation irradiation to evaluate the charge recombination patterns in the TiO_2/SiO_2, 2_S_TiO_2/SiO_2 and 4_S_TiO_2/SiO_2 samples.

2.4. Experimental unit

The experiments to evaluate the photocatalytic activity of the synthesized materials were carried out in a borosilicate glass gas-solid photocatalytic reactor (GSPR) with a height of 120 mm and an internal diameter of 4 mm. Glass wool was placed at the top and bottom ends of the tube to retain the photocatalytic material. The irradiated section of the reactor was consistently filled with solids in all tests, creating a 7 cm high bed (equivalent to an irradiated volume of 1.5 mL). This ensured that the only variable in the experiments was the photocatalytic material. The reactor, housed inside a cabinet designed for photocatalytic tests (Fig. 1), received a gaseous stream of pure oxygen from a cylinder. This stream was split into three: the first passed through a water bubbler to regulate humidity, the second carried pure oxygen, and the third was directed through a 5-mm inner diameter *n*-hexane diffusion tube, immersed in a 5 °C thermostatic bath to control the inlet *n*-hexane concentration based on the bath temperature. All three oxygen flows were monitored continuously by mass flow meters (D6FP0001A1, Omron) in the range of 0–100 mL min^{-1}. The gas stream temperature, maintained between 20 and 25 °C, and humidity were measured by an ITHT2210 hygrometer (Instrutemp) at the entrance to the glass reactor.

To evaluate the photocatalytic activity, the reactor was exposed to an irradiation source consisting of a high-power metal halide lamp (400W HPI-T, Phillips Co.) positioned 18 cm from the reactor (Fig. 1) to obtain UV irradiance equivalent to that of the ASTM AM1.5G standard AM 1.5G solar spectrum at sea level, approximately 4.6 mW cm^{-2}, in the same wavelength range (300–400 nm). The irradiance spectra of the light source on the reactor surface were measured using a spectroradiometer (SPR-4002, Luzchem Research, Inc.).

The initial set of experiments involved maintaining fixed operating conditions (relative humidity, irradiance, and inlet *n*-hexane concentration at 50 %, 4.6 mW cm^{-2}, and 80 ppm, respectively). The catalyst sample inside the reactor was then altered to assess how the different sulfur contents added in the synthesis influenced the photocatalytic performance. Subsequently, tests were conducted, varying the operating conditions of relative humidity (0, 50, and 100 %) and in the absence of oxygen in the gas stream, i.e., N_2 gas, keeping the other operating conditions constant. Finally, the stability of the material that exhibited the greatest photocatalytic activity was assessed by a 180-min test. All tests were carried out in duplicate to validate the results obtained.

For the photocatalytic tests, a 60-min dark equilibrium adsorption phase was initiated. The light source was then switched on for a sufficiently long period to reach a stabilized *n*-hexane concentration at the reactor outlet. This concentration was monitored continuously using an in-line GC-PID/TiD gas chromatograph (Meta) at 2-min intervals. The GC-PID/TiD analyzed a 98-μL sample injected through a Restek RTX-Volatiles column (30 m, 0.32 mm i.d., 2.0 μm thick) with N_2 as the

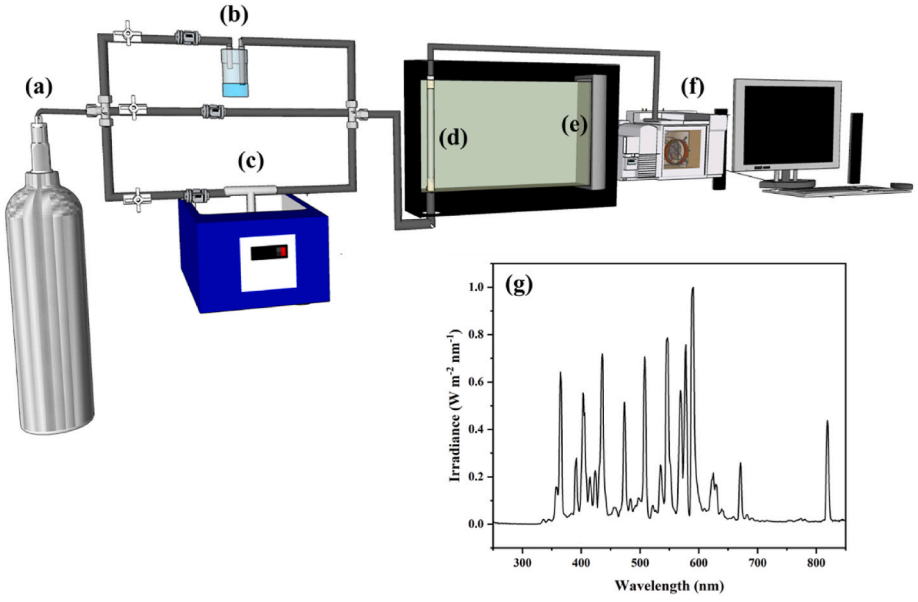

Fig. 1. Description of the experimental unit: a) Oxygen cylinder; b) Humidifier; c) *n*-hexane diffusion tube; d) GSPR; e) High-power metal halide lamp; f) GC-PID/TiD gas chromatograph; g) Irradiance spectra of the light emitted by the 400W HPI-T lamp at the same distance from the reactor.

carrier gas. The oven temperature was kept at 70 °C without a heating ramp. The *n*-hexane content in the gas stream was quantified using a photoionization detector equipped with a Krypton gas lamp (10.6 eV) and operated at a temperature of 200 °C. After five consecutive analyses on the in-line GC-PID/TID indicating stability, the light source was switched off again until the outlet *n*-hexane concentration stabilized. Subsequently, the radiation source was switched on again, repeating the same cycle three times to ensure the reproducibility of the results.

The evaluation of the different photocatalytic tests involved examining the steady-state conversion of *n*-hexane, denoted as X (according to Eq. (1)), and the apparent reaction rate, denoted as R (as per Eq. (2)). In these equations, C_i and C_0 represent the steady-state inlet and outlet *n*-hexane concentrations in the reactor, respectively. The gas flow rate through the reactor is represented by Q, and m stands for the mass of TiO_2.

$$X = \frac{C_i - C_0}{C_i} \tag{1}$$

$$R = \frac{Q \times (C_i - C_0)}{m} \tag{2}$$

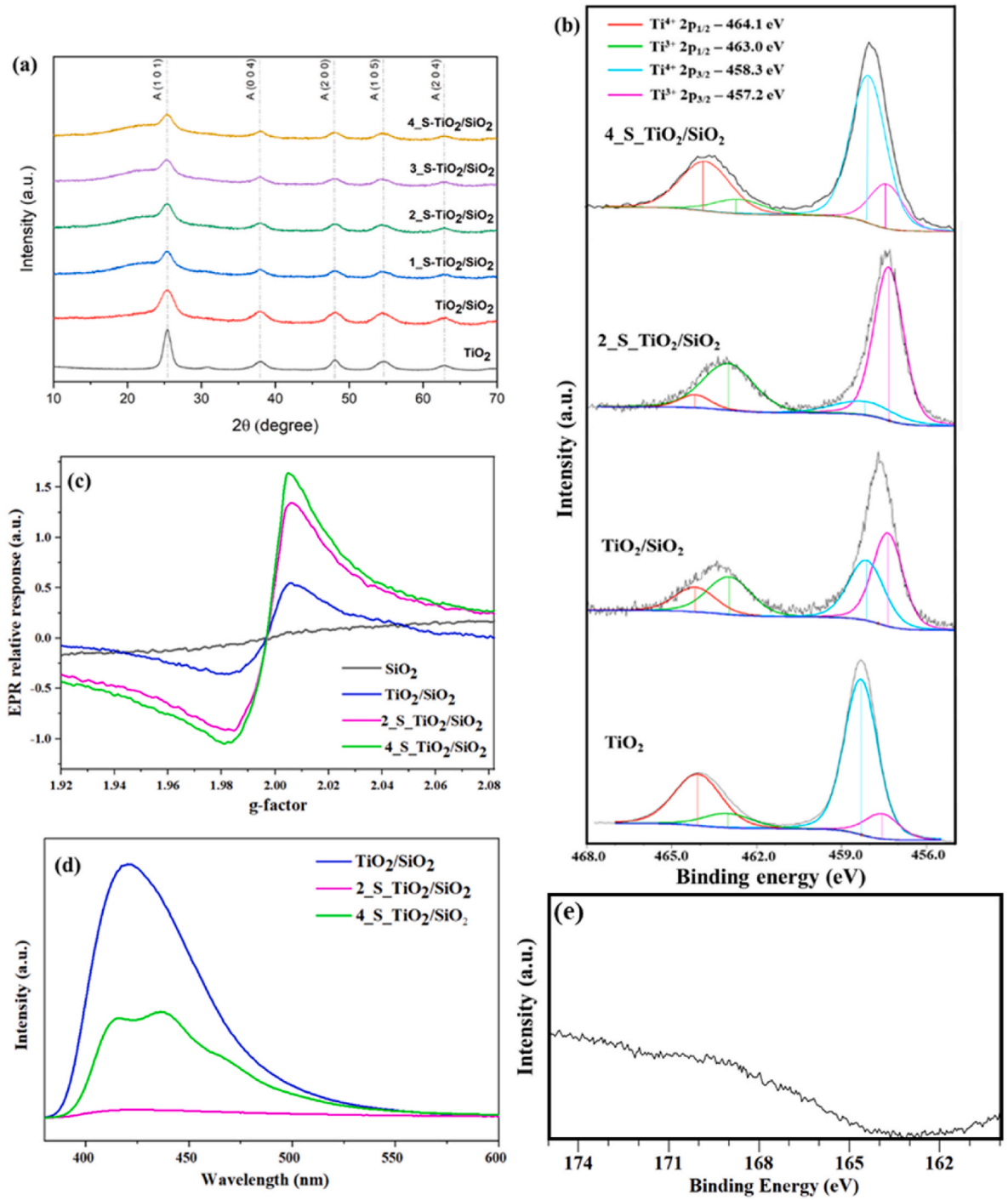

Fig. 2. (a) XRD diffractograms of the synthesized materials; (b) High resolution Ti 2p spectra of TiO_2, TiO_2/SiO_2, 2_S_TiO_2/SiO_2 and 4_S_TiO_2/SiO_2; (c) EPR spectra of SiO_2, TiO_2/SiO_2, 2_S_TiO_2/SiO_2 and 4_S_TiO_2/SiO_2; (d) PL spectra of TiO_2/SiO_2, 2_S_TiO_2/SiO_2 and 4_S_TiO_2/SiO_2; (e) High resolution S 2p spectra of 2_S_TiO_2/SiO_2.

3. Results and discussion

3.1. Characterization

Fig. 2a shows the XRD patterns of pure TiO_2, TiO_2/SiO_2 and the sulfur-doped materials at different contents. The diffractograms indicate only peaks referring to the anatase crystalline phase, with the most intense peaks at $2\theta = 25$, 48 and 63°, which refer to the (101), (200) and (204) crystallographic planes, respectively, according to JCPDS card no. 96-720-6076. The diffractograms also show peaks at $2\theta = 37°$, which can be attributed to the crystallographic planes (103), (004), and (112), and 55°, which can be associated with the (105) and (211) anatase planes. Due to the irregular polycrystalline structure of the material, it is possible that these peaks actually result from an overlap of the mentioned planes [16,17]. The use of silica gel as a support significantly reduced the crystallinity of the material, as can be observed by a broad base corresponding to the presence of amorphous SiO_2 [16,18]. The TiO_2 crystallite sizes were determined by the Scherrer Equation (Eq. (3)), where $k = 0.89$ is the shape factor, λ is the wavelength of the X-ray radiation (Cu Kα = 0.154056 nm), β is the full-width half-maximum (FWHM) of the diffraction peak and θ is the X-ray diffraction angle.

$$D = \frac{k \times \lambda}{\beta \times \cos\theta} \quad (3)$$

Table 1 shows that the calculated mean crystallite size slightly decreased from 5.2 nm to 4.3 as the material was supported on SiO_2, which is consistent with our previous report [16]. This was expected due to the presence of Si−O−Si bonds, which decrease the interaction between the TiO_2 nanoparticles, thereby slowing down crystal growth [19]. In addition, it is possible that silica was segregated into TiO_2 during its crystallization, thereby slowing down the growth of the semiconductor crystals [20]. Furthermore, the XRD pattern remained unchanged with the gradual addition of the sulfur precursor, indicating that sulfur did not induce the formation of other crystalline phases. Table 1 shows that the average size of the TiO_2 crystallite increased slightly with the addition of the sulfur precursor.

The sulfur contents determined through energy dispersive X-ray spectroscopy indicated that virtually all the sulfur introduced into the materials using thiourea was lost during the drying and calcination stages. The loss of sulfur content increased in line with the gradual increase in the mass of thiourea added in the synthesis, as shown in Table 1. It is therefore unlikely that these changes in crystallite size are due to the incorporation of sulfur into the TiO_2 crystal lattice. Other characterization techniques that will be discussed later in this work directly support this hypothesis.

XPS analysis was carried out to evaluate the influence of using silica gel as a support, as well as the addition of sulfur in the synthesis of materials on surface speciation. Fig. 2b shows a comparison of the high-resolution XPS spectra of Ti 2p for the pure TiO_2, TiO_2/SiO_2, 2_S_TiO_2/SiO_2 (the material which exhibited the best photocatalytic performance) and 4_S_TiO_2/SiO_2, synthesized with the highest thiourea content. When comparing the spectra of the materials, there is a blue shift of the two bands corresponding to Ti $2p_{1/2}$ and Ti $2p_{3/2}$, from pure TiO_2 to TiO_2/SiO_2 and even more prominently from TiO_2/SiO_2 to 2_S_TiO_2/SiO_2. This behavior becomes clearer by comparing the deconvoluted spectra, considering the bands for Ti^{4+}-O (464.1 and 458.3 eV for Ti $2p_{1/2}$ and Ti $2p_{3/2}$, respectively) and Ti^{3+}-O (463.0 and 457.2 eV for Ti $2p_{1/2}$ and Ti $2p_{3/2}$, respectively) [7]. Table 2 shows the percentages of each peak in the deconvolution. While the peaks referring to lattice Ti^{3+} corresponded to only 19.2 % for pure TiO_2, they reached 58.4 % for TiO_2/SiO_2 and 83.2 % for 2_S_TiO_2/SiO_2, clearly indicating that the sulfur precursor in the synthesis induced the reduction of Ti^{4+} to Ti^{3+} on the surface of the material. Sahu et al. [21] demonstrated that thiourea, which contains sulfur and nitrogen atoms, is highly susceptible to oxidation by a wide range of oxidizing agents, generating various products such as sulfides, sulfur oxides and nitrogen oxides. It is therefore possible that the oxidation of thiourea has produced volatile products, such as sulfur oxides, while removing electrons from TiO_2, explaining the reduction of Ti^{4+} to Ti^{3+}, as well as the loss of sulfur from the material. The creation of oxygen vacancies is explained by the crystal structure of TiO_2, in which the unsaturated bridging oxygen atoms have double coordination, so that they can be easily removed from the lattice in the calcination step. In this way, oxygen vacancies are generally regarded as the most reactive sites in TiO_2 [22,23]. Fig. 3 illustrates a mechanism for doping TiO_2 with Ti^{3+} by adding thiourea during the material synthesis.

On the other hand, Fig. 2e shows the high-resolution XPS spectrum of the S 2p region for the 2_S_TiO_2/SiO_2 sample, in order to assess the presence and quantify the sulfur species on the catalyst surface. Only noise was shown in the S 2p spectra, indicating the absence of sulfur on the surface of the materials, as revealed in the EDX analysis (Table 1). During the calcination step, due to the high reaction temperature (450 °C) for 240 min, it is suggested that the sulfur was released from the material as oxides (SO_3 and SO_2).

Studies have already shown that the generation and location of defects on the surface of the material are highly dependent on the synthesis route and conditions. In this sense, the synthesis of the so-called "black TiO_2" using the approach described in this article appears to be an innovative and attractive alternative. In this methodology, the generation of crystal defects occurs during the calcination stage at moderately low temperatures, in which only the surface of the TiO_2 is likely to undergo the chemical transformations that lead to the formation of oxygen vacancies and Ti^{3+} centers [20].

Fig. 2b shows the high-resolution Ti 2p spectrum for the 4_S_TiO_2/SiO_2 material. Increasing the sulfur content reduced the percentage of Ti^{3+} from 83.2 to 44.4 % on the crystal surface (Table 2). It is suggested that the excessive thiourea content added in the synthesis stage before calcination resulted in the migration of the sulfur atoms to the grain boundary in order to minimize the energy of the system. At low contents, thiourea plays a minor role in the relative stability of the interfaces; but, as the crystal lattice becomes saturated with sulfur, changes in the stability of the interfaces begin to appear due to the segregation of the dopant, mainly at the grain boundaries, in order to energetically stabilize the system [20]. Therefore, the generation of oxygen vacancies and Ti^{3+} was mainly driven by the sulfur segregated at the grain boundaries,

Table 2
Deconvoluted Ti 2p peaks from high-resolution XPS spectra.

Material	Ti^{4+} (%)	Ti^{3+} (%)
TiO_2	80.8	19.2
TiO_2/SiO_2	41.6	58.4
2_S_TiO_2/SiO_2	16.8	83.2
4_S_TiO_2/SiO_2	55.6	44.4

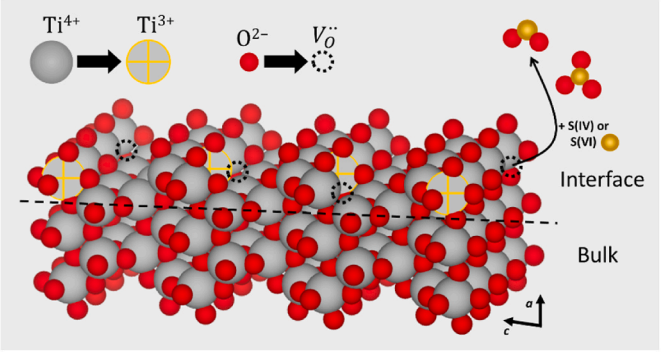

Fig. 3. Illustration of the formation of vacancies and reduced titanium species on the surface of the S_TiO_2/SiO_2 material.

which explains the low amount of Ti^{3+} on the surface of the material [20].

EPR characterization was applied to assess the presence of crystalline defects, specifically oxygen vacancies. Fig. 2c shows the comparison between the EPR spectra of the materials TiO_2/SiO_2, 2_S_TiO_2/SiO_2 and 4_S_TiO_2/SiO_2 to evaluate the effect of thiourea content on the generation of crystalline defects in TiO_2. The analysis provides valuable insights into the crystalline defects found in the bulk of TiO_2 and not just on the surface. Previous studies have already revealed that the ratio of defects in the bulk to those on the surface is a determining factor in

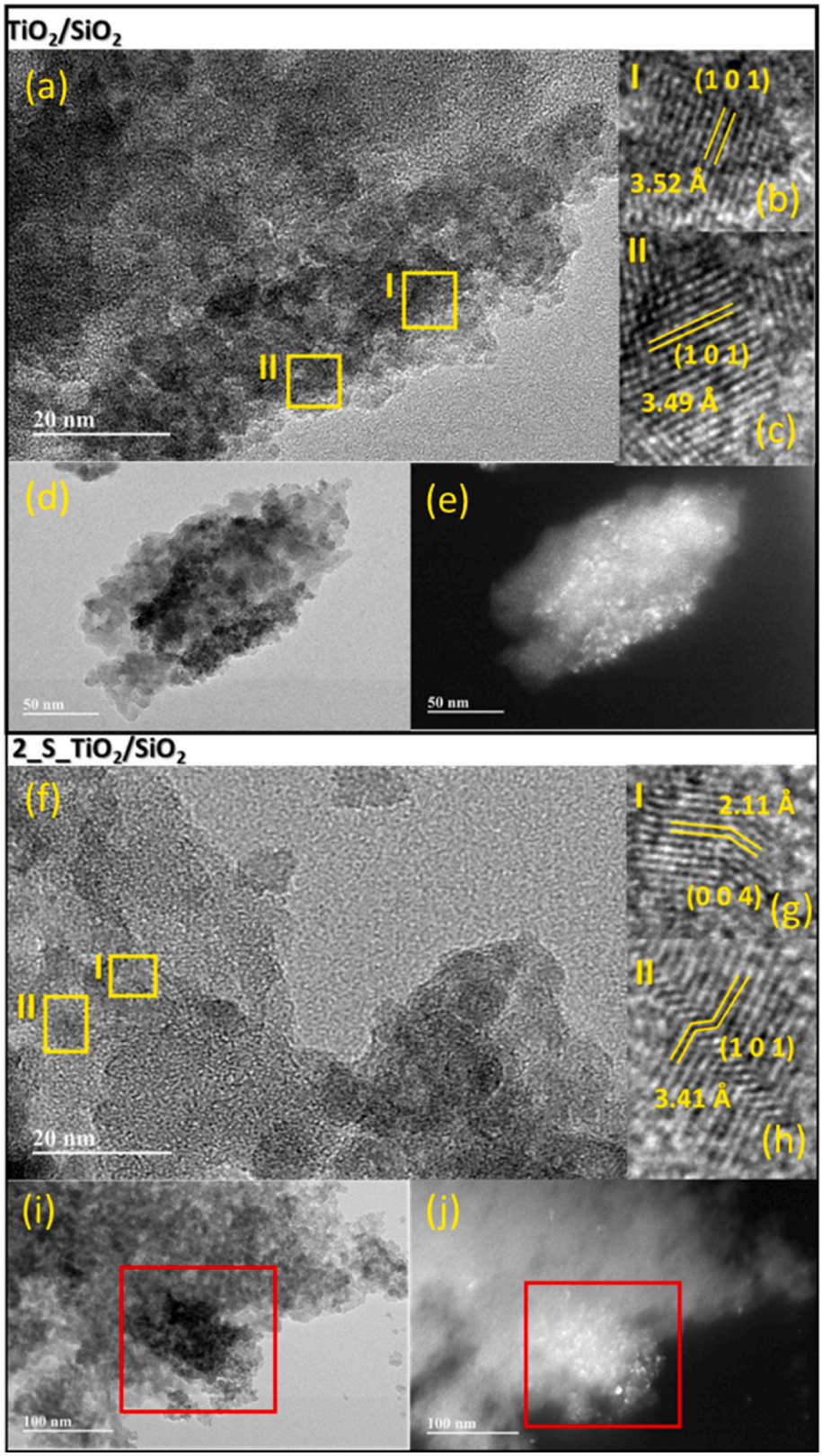

Fig. 4. (a, b, c) HRTEM image of TiO_2/SiO_2; (d, e) TEM images of TiO_2/SiO_2; (f, g, h) HRTEM image of 2_S_TiO_2/SiO_2; (i, j) TEM images of 2_S_TiO_2/SiO_2.

improving or suppressing the photocatalytic activity of the material, since defects in the bulk act as charge recombination centers whereas those on the surface aid in the separation of photogenerated charges, and also act as adsorption centers [24–27]. It can be seen that the EPR signal increased with the addition of sulfur during synthesis, indicating a greater density of oxygen vacancy defects in the material [28]. Previous studies reported different values for the g-factor corresponding to surface and bulk Ti^{3+}, but in general values of g = 1.94 to −1.99 are assigned to bulk Ti^{3+} and g = 2.01 to −2.02 to surface Ti^{3+} defects [24,28,29]. Similarly, the g-factors = 1.99, 2.01 and 2.00 are also assigned to oxygen vacancies. It should be noted that these values are typical of Ti^{3+} defects under experimental conditions of EPR analysis close to T = 20 K [30]. The results suggest that the increase in the intensity of the g = 1.99-factor corresponds to a greater density of oxygen vacancies.

Comparing the results obtained in the EPR and XPS analyses, the 2_S_TiO_2/SiO_2 catalyst, synthesized with a lower sulfur precursor content, showed a higher proportion of Ti^{3+} on the surface compared to the TiO_2/SiO_2 sample. However, when the 2_S_TiO_2/SiO_2 sample is compared with the 4_S_TiO_2/SiO_2 sample, there is an increase in the density of oxygen vacancies in the bulk, according to the EPR analysis, but a reduction in the proportion of Ti^{3+} defects on the surface.

Although an assertive location of crystalline defects in complex materials such as those reported in this work requires more sophisticated techniques, the XPS and EPR results discussed together suggest that at high thiourea contents, the dopant has indeed segregated at the bulk or grain boundaries. Therefore, despite having a higher density of oxygen vacancies, its surface is poor in defects, which could significantly impact the photocatalytic activity of the material. The increase in the density of crystalline defects, proportional to the amount of sulfur precursor added in the synthesis, may explain the observed increase in crystal size as determined by X-ray diffraction (XRD) analyses. The defects promote atoms diffusion within the crystal, typically favoring crystallite growth [31].

Photoluminescence analysis was performed to support the XPS and EPR findings, since the presence of defects plays an important role in the efficient separation of photogenerated charges, and the intensity of the photoluminescence emission spectrum is closely related to that photogenerated charge separation [32]. The photoluminescence spectrum of the TiO_2/SiO_2 sample (Fig. 2d) showed the highest intensity, contrasting with the 2_S_TiO_2/SiO_2 sample, characterized by a significant proportion of Ti^{3+} defects as revealed by XPS. Notably, as shown in Fig. 2d, the 4_S_TiO_2/SiO_2 material, featuring the highest overall oxygen vacancy density, exhibited an intermediate photoluminescence intensity. Although exceeding that of the 2_S_TiO_2/SiO_2 sample, the photoluminescence intensity of the 4_S_TiO_2/SiO_2 catalyst was notably lower than that of bare TiO_2/SiO_2, suggesting that the material with the higher sulfur content suffered greater charge recombination than the 2_S_TiO_2/SiO_2 sample, but less than TiO_2/SiO_2. This suggests that, even with higher than ideal thiourea contents, the addition of the sulfur precursor reduces the photogenerated charge recombination [26,27].

Transmission electron microscopy (TEM) was used to assess the distribution of TiO_2 nanoparticles on the silica surface and to determine the crystallographic planes of anatase in the sample. The TiO_2/SiO_2 composite revealed silica grains adorned with numerous TiO_2 nanoparticles, as shown in Fig. 4d. A comprehensive examination of the dark and bright field images (Fig. 4d and e) of the same sample provides valuable insights, notably discernible by the presence of several bright spots characteristic of TiO_2 superimposed on an opaque silica surface. Dark field images further unveil the agglomeration of TiO_2 nanoparticles due to particle overlapping. To investigate the crystallographic features, the d-spacing of the planes was calculated using Fourier Transform analysis at select locations within the HRTEM image (Fig. 4a). The resulting frequency spectrum showed distinct lattice spacings, all consistently indicative of the (101) crystallographic plane. This observation aligns with the diffractogram of the sample, revealing the highest intensity for the (101) plane. The lattice spacing values calculated (3.52 and 3.49 Å) were close to the standard values (3.520 Å), as shown in Fig. 4b and c.

Transmission Electron Microscopy (TEM) and High-Resolution Transmission Electron Microscopy (HRTEM) images of the 2_S_TiO_2/SiO_2 sample were also acquired for comprehensive characterization. The lattice spacings were computed from selected points in Fig. 4f, revealing distinct features corresponding to the (101) and (004) crystallographic planes. This observation is in line with the corresponding diffractogram, in which the most intense peaks were consistently assigned to these specific planes. Interestingly, the calculated lattice spacing values (2.11 Å and 3.41 Å) exhibited a slightly widened deviation from the standard values (2.378 Å and 3.520 Å) compared to the TiO_2/SiO_2 sample discussed previously [16]. The challenges posed by nanoparticle overlap and the polycrystalline nature of the sample, supported on silica, make it intricate to pinpoint and discuss crystalline defects unequivocally using HRTEM images, given the number of variables that can influence the results. This highlights the need for a holistic interpretation, incorporating complementary techniques such as the X-ray Photoelectron Spectroscopy (XPS) and Electron Paramagnetic Resonance (EPR) discussed earlier. Nevertheless, intriguing observations emerge from Fig. 4g (Image I) and 3h (Image II). Image I reveals a discernible step, suggestive of possible crystalline defects such as discordances or atomic dislocations [5,33]. In Image II, a likely grain boundary is identified, characterized by a perceptible discontinuity in the orientation of crystallographic planes. Fig. 4i and j juxtapose dark-field and bright-field imaging, revealing a localized concentration of TiO_2 nanoparticles in a distinct region of the silica particle. This is in stark contrast to the TiO_2/SiO_2 sample, where the distribution of TiO_2 nanoparticles exhibited a more uniform coverage of the silica surface.

Furthermore, scanning electron microscopy analyses of the TiO_2/SiO_2, 2_S_TiO_2/SiO_2, and 4_S_TiO_2/SiO_2 samples generally show particle heterogeneity, as shown in Fig. 5a, b and c. Part of the TiO_2 nanoparticles is supported on silica grains. The images also reveal clusters of TiO_2 nanoparticles, especially in samples that contain sulfur in their formulation. In the synthesis step, it is hypothesized that the presence of sulfur compounds promoted the acidification of the aqueous medium and made it difficult to attain the necessary zeta point for the TiO_2 particles to adhere satisfactorily onto the silica [34]. The EDS spectra of specific points were analyzed (Fig. 5g), as shown in Fig. 5d, e, and f. Interestingly, although XPS did not detect sulfur on the TiO_2 surface, the EDS spectrum identifies a trace of sulfur, especially in the sample with the highest concentration of the non-metal. It is noteworthy that sulfur characteristic peaks were only identified when points were selected in the image above the TiO_2 nanoparticles. On the silica surface, the EDS analysis did not detect sulfur, indicating that the remaining non-metal in the sample is concentrated in the semiconductor.

Fig. 6a shows the UV–Vis absorption spectra of the samples. It can be seen that, at wavelengths up to 400 nm, the sulfur-doped materials exhibited a much stronger absorbance compared to the TiO_2/SiO_2 materials, with the 2_S_TiO_2/SiO_2 sample showing the highest absorbance in the visible light range. The increase in the UV–VIS absorbance of the sulfur-doped materials can be attributed to the reduction in the band gap resulting from the formation of crystal defects [5]. Each oxygen vacancy leaves two valence electrons, which then occupy the empty Ti 3d levels, generating energy levels situated below the conduction band (CB) [23]. The typical bandgap of TiO_2 crystals is approximately 3.2 eV (UV absorption). The presence of defects, such as oxygen vacancies and Ti^{3+}, can effectively narrow this bandgap by introducing additional electronic levels within it [24,35]. The existence of excess electrons, originating from oxygen vacancies and Ti^{3+}, imparts an n-type conductivity to TiO_2. In undoped TiO_2, lacking vacancies and defects, the Fermi level resides at the midpoint of the bandgap at 0 K. For n-type TiO_2 (with excess electrons from donor impurities), the Fermi level shifts towards the CB, while for p-type TiO_2 (with more holes from acceptor impurities), it shifts towards the valence band (VB). With the n-type characteristic of modified TiO_2, the Fermi level will be observed in the vicinity of the CB

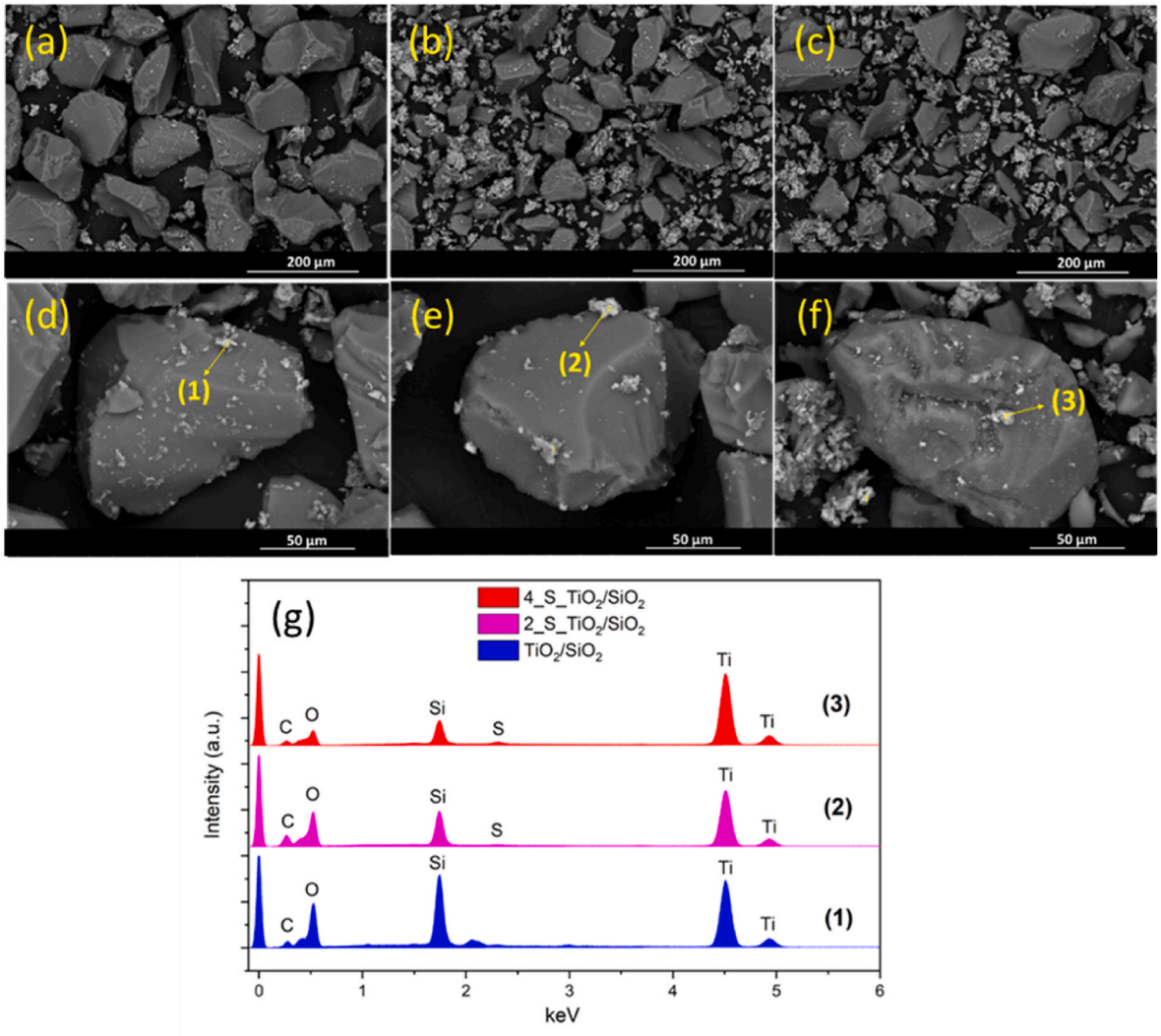

Fig. 5. SEM and EDS spectra results.

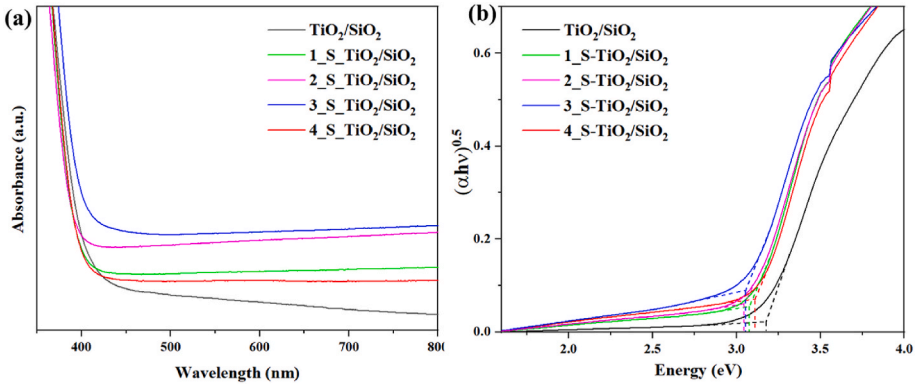

Fig. 6. (a) UV–VIS spectra and (b) Tauc plot of the synthesized materials.

[23]. In the present work, the band gap energies of the synthesized materials were estimated using the Tauc method, extrapolating the tangent line to the inflection point of the curve to intersect with the x-axis. The Tauc method applies Eq. (4), where α is the absorption coefficient, $h\nu$ (eV) is the energy associated with the wavelength ($h\nu = 1240/\lambda$), B is the proportionality constant, E_g is the bandgap energy, and n is a variable dependent on the nature of the semiconductor (direct or indirect). In this case, where TiO_2 is a direct semiconductor, n is equal to 2 [16,36]. Fig. 6b shows the Tauc plots of the different materials synthesized, and Table 1 presents the corresponding band gap energies, highlighting the reduction in band gap energy with the incorporation of crystal defects into the materials.

$$(\alpha h\nu)^{\frac{1}{n}} = B\left(h\nu - E_g\right) \tag{4}$$

Equations (5) and (6) were used to calculate the E_{CB}, E_{VB} and E_g values, which represent the respective positions of the conduction and valence band levels, as well as the band gap energy. In this context, E_e means the energy of the free electron (4.5 eV vs. SHE), while χ denotes the electronegativity of the semiconductor material, which for TiO_2 is 5.84 eV. This value is equivalent to the geometric mean of the electronegativities of its constituent atoms [37]. The valence and conduction band potentials of the synthesized catalysts using different thiourea contents are shown in Table 1.

$$E_{VB} = \chi - E^e + 0.5 \times E_g \quad (5)$$

$$E_{CB} = E_{VB} - E_g \quad (6)$$

As the potentials in the conduction band of all the synthesized materials (Table 1) were more negative than those for oxygen reduction ($O_2/O_2^{\bullet-}$: −0.16 eV vs. SHE) [38], it is believed that the electrons in the conduction band are effective in reducing gaseous oxygen to superoxide radicals. Meanwhile, the positive holes in the valence band can oxidize water molecules ($H_2O/^{\bullet}OH$: 2.72 eV vs. SHE) or hydroxide anions ($OH^-/^{\bullet}OH$: 2.40 eV vs. SHE) that are adsorbed on the surface of the material. This interaction leads to the formation of $^{\bullet}OH$ radicals, as reported in previous studies [39], which contribute to the photocatalytic oxidation of volatile organic compounds.

3.2. Photocatalytic performance of the synthesized materials

The photocatalytic performance of the different synthesized materials was tested by the degradation of *n*-hexane (selected as a model volatile organic compound) under UV–VIS radiation, and the results are shown in Fig. 7a and Table 3. The TiO_2/SiO_2 sample exhibited 34.2 % *n*-hexane removal under these conditions. As elucidated in the characterization results discussed earlier, the UV–VIS spectrum of the sample indicated a limited capacity to absorb radiation beyond 380 nm. Despite this constraint, it is worth noting that solar radiation encompasses a fraction of the ultraviolet radiation (4.6 mW cm^{-2}) that the TiO_2/SiO_2 photocatalyst is capable of absorbing. This observation rationalizes the photocatalytic efficiency observed, underscoring the importance of its performance under solar irradiation.

Table 3
Evaluation of the photocatalytic activity of the synthesized materials under different operating conditions.

Material	Relative humidity (%)	Presence of oxygen	*n*-hexane degradation (%)	Reaction rate (μmol $gTiO_2^{-1}$ h^{-1})
TiO_2/SiO_2	50	✓	34.2	10.8
1_S_TiO_2/SiO_2	50	✓	40.1	12.8
2_S_TiO_2/SiO_2	50	✓	61.2	20.5
3_S_TiO_2/SiO_2	50	✓	45.6	14.4
4_S_TiO_2/SiO_2	50	✓	36.9	11.7
2_S_TiO_2/SiO_2	50	X	14.9	4.7
2_S_TiO_2/SiO_2	0	✓	78.8	26.0
2_S_TiO_2/SiO_2	100	✓	3.7	1.2
TiO_2/SiO_2	0	✓	29.1	9.2
TiO_2/SiO_2	100	✓	24.7	7.8

The 2_S_TiO_2/SiO_2 material showed the highest photocatalytic activity, as evidenced by the 61.2 % degradation of *n*-hexane (Table 3). As shown by XPS, PL and EPR, this increase in the photocatalytic performance of the material may be related to the presence of crystalline defects, especially Ti^{3+} and oxygen vacancies. Initially, the presence of oxygen vacancy defects holds significant importance in promoting surface activation and the adsorption of gas molecules. As the photocatalytic system investigated in this study operates in the gas phase, it is

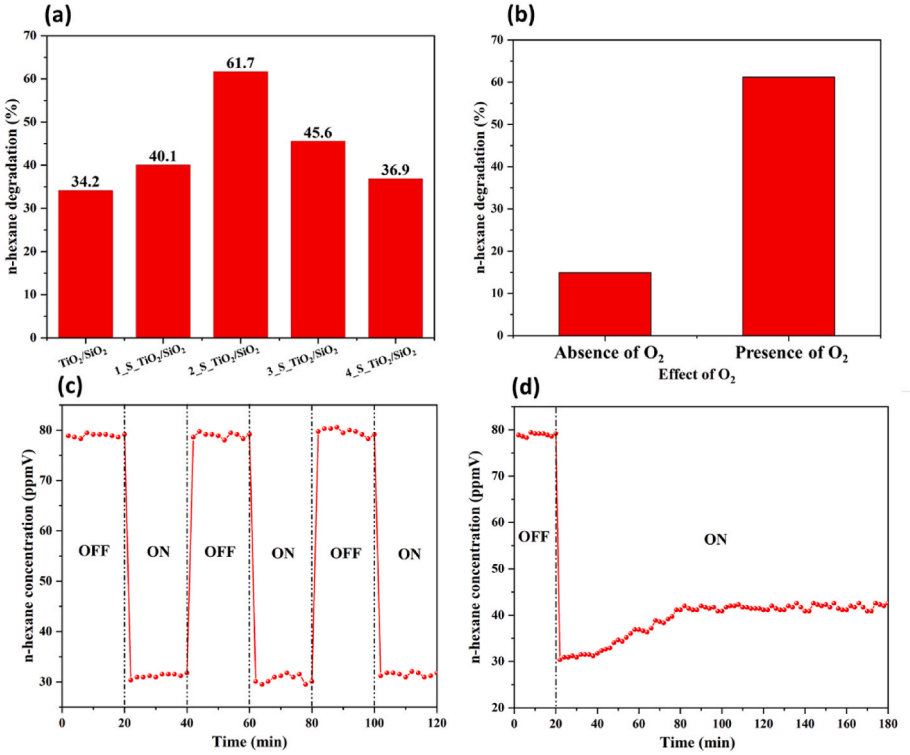

Fig. 7. (a) Comparison of *n*-hexane degradation obtained for the synthesized materials; (b) Comparison of *n*-hexane degradation for 2_S_TiO_2/SiO_2 in the absence and presence of O_2 in the gas stream; (c) Evolution of *n*-hexane degradation in three cycles with and without irradiation for 2_S_TiO_2/SiO_2; (d) Evaluation of the photoactivity stability of 2_S_TiO_2/SiO_2 over 180 min.

proposed that the existence of oxygen vacancies facilitated the adsorption of both contaminant molecules on the active sites of the catalyst, as well as the adsorption of water and oxygen [6].

In addition, surface oxygen vacancy defects have the ability to capture electrons or holes through their defect energy state levels, thereby expediting the migration of carriers towards adsorbates. Moreover, the higher density of oxygen vacancies in the bulk may have contributed to an expansion of the light absorption spectrum of the material, as demonstrated by the results of the UV–VIS analysis. The presence of Ti^{3+} on the surface also plays a fundamental role in enhancing photocatalytic activity. The creation of Ti^{3+} induced new electronic levels below the conduction band, leading to band gap narrowing and consequent visible light activity [5,6,23,24].

On the other hand, the materials with the highest sulfur content added in the synthesis showed a decrease in photocatalytic activity (36.9 %), as shown in Table 3. As shown by the EPR, XPS and PL characterization results, the 4_S_TiO_2/SiO_2 material had a higher density of oxygen vacancies in the bulk, but a lower proportion of Ti^{3+} on the surface. In addition, the photoluminescence results showed an increase in charge recombination for this material. Our research findings therefore suggest that not only the concentration, but also the location of the defects significantly influences photocatalytic activity. Specifically, surface oxygen vacancies are believed to play a role in the separation of photogenerated charge carriers, while an overabundance of bulk oxygen vacancies has been observed to act as recombination centers [25–27, 37]. In addition, previous research has indicated that an excess of oxygen vacancies on the surface can capture electrons, hindering the conversion of adsorbed oxygen molecules into $O_2^{\bullet-}$ for the degradation of *n*-hexane [23,24].

Subsequently, an assay was conducted to evaluate the role of oxygen gas in *n*-hexane photocatalytic degradation. For this purpose, an experiment was carried out, maintaining all the experimental conditions, but using nitrogen gas instead of oxygen gas as carrier gas. Fig. 7b compares the degradation efficiency in the reaction with and without oxygen. There was a significant reduction from 61.2 % to 14.9 % in the absence of O_2, as shown in Table 3.

This underscores the pivotal role of gaseous oxygen in the degradation mechanism, as it forms superoxide radicals and atomic oxygen species crucial to the process. This inference is supported by the band energy estimates (Table 1), revealing the effectiveness of conduction band electrons in reducing oxygen to $O_2^{\bullet-}$ radicals. However, there was still a significant removal of the contaminant (14.9 %) in pure nitrogen, suggesting alternative degradation pathways, including the generation of hydroxyl radicals resulting from the interaction between water molecules and/or HO^- with positive holes, which was also demonstrated by calculations of conduction and valence band potentials [36,39]. In addition, previous studies have shown that under these conditions, the presence of pure nitrogen can lead to the formation of reactive nitrogen species (RNS), such as N_2 ($C^3\prod_u$), N_2 ($B^3\prod_g$), and metastable nitrogen states, which may also participate in degradation reactions [40].

Fig. 7c depicts the evolution of *n*-hexane concentration over three reaction cycles with and without irradiation for the test carried out with the 2_S_TiO_2/SiO_2 catalyst, suggesting that the conversion remained stable throughout the cycles. Photocatalytic tests were then carried out under the same operating conditions for a longer period of time using the catalyst that exhibited the highest photocatalytic activity, in order to assess the stability of the material. Photocatalytic deactivation constitutes a significant concern that could prevent the widespread application of this technology for the large-scale removal of VOCs [16]. Deactivation is usually associated with the chemical adsorption of intermediate and persistent organic compounds formed on the surface of the photocatalyst [41]. As illustrated in Fig. 7d, the activity of the photocatalyst remained almost constant for several hours of the reaction, indicating the absence of persistent intermediate by-products during the degradation of *n*-hexane. After 80 min, the conversion gradually declined to approximately 50 %, remaining at this level until the end of the test, which lasted for 180 min. Deactivation of TiO_2 in photocatalytic processes generally occurs in reactions involving aromatic, nitrogenous and chlorinated compounds, phenomena that are not anticipated for single-chain alkane hydrocarbons such as *n*-hexane [41].

Finally, as shown in Fig. 7c, the decay in the hexane outlet concentration is virtually instantaneous upon irradiation. A simple kinetic modelling based on the Langmuir-Hinshelwood model (Text S1) retrieves a reaction rate constant of 43.92 μmol g^{-1} h^{-1} and an adsorption equilibrium constant of 0.286 m^3 $mmol^{-1}$, for the space time of the experiment (4.7 s). The adsorption equilibrium constant was close to the value found in the adsorption analysis of a similar system (n-heptane on TiO_2), of 0.31 m^3 $mmol^{-1}$ [42], in close correspondence with the observation by Matsumoto et al. [43] for the degradation kinetics of hexane in a fluidized bed photocatalytic reactor (0.109 m^3 $mmol^{-1}$), and ca. One order of magnitude higher than that found for *n*-hexane at higher inlet concentrations, ca. 0.023 m^3 $mmol^{-1}$ [44]. This difference can be attributed to the nature of adsorption in the gas phase, which is highly dependent on parameters such as surface velocity, bed porosity, and humidity. The reaction rate constant is considerably lower than that observed in UV-C reactors with better irradiation distribution, with values in the order of several mmol g^{-1} h^{-1} being reported [45]; but it is higher than the values observed for reactors with coated walls, as in the work by Boulamanti and Philippopoulos [46], where a reaction rate of 2.2×10^{-2} μmol g^{-1} h^{-1} was found. The wide range of results emphasizes the importance of light transport and reactor design control.

3.2.1. The role of the relative humidity in the gas stream

The study of the effect of relative humidity in the gas stream in this same reaction system has already been carried out in a previous work, using TiO_2/SiO_2 as a catalyst. In that study, the relative humidity was varied by 0, 50 and 100 % and there was no considerable influence on the degradation of *n*-hexane [16]. However, in the present study, the same study was carried out using the 2_S_TiO_2/SiO_2 catalyst and the behavior was completely different from that of the pure material, as shown in Fig. 8a. While the test carried out at 0 % relative humidity showed 78.8 % degradation, the test carried out at 100 % relative humidity showed only 3.7 % degradation of the contaminant (Table 3).

In the presence of oxygen vacancies on the surface, as evidenced by the characterization analyses of the 2_S_TiO_2/SiO_2 material, the adsorbed water molecules occupy these vacancies, resulting in a highly hydrophilic surface. This suggests that the oxygen vacancies on the modified catalyst surface have led to hyperhydrophilicity, where the water molecules strongly adhere, hindering the diffusion of contaminant molecules to the active sites [47]. Even with an inlet relative humidity of 0 %, the strong interaction of water molecules means that there is still residual water adsorbed on the catalyst, influencing the reaction; but there is no excess water to saturate the surface and prevent the diffusion of hexane. On the other hand, at 100 % humidity, the water is strongly adsorbed, preventing the contaminant from reaching the active sites (Fig. 8c).

To substantiate these findings, an FTIR spectrum was acquired on the TiO_2/SiO_2 and 2_S_TiO_2/SiO_2 materials (Fig. 8b). After 24 h in an oven at 80 °C to desorb the water from the surface, the results reveal that water is still highly adsorbed on the surface of the 2_S_TiO_2/SiO_2 sample, based on the two distinctive bands of adsorbed water at 1635 cm^{-1} (O−H benching) and 3360 cm^{-1} (O−H stretching), confirming the hyperhydrophilic nature of the material [48].

3.2.2. Photocatalytic mechanism

Based on the various experimental conditions investigating relative humidity and the presence of oxygen, together with estimates of the conduction and valence band potentials of the synthesized materials, a comprehensive photocatalytic mechanism was proposed for the 2_S_TiO_2/SiO_2 material, as shown in Fig. 9. The oxygen vacancies act as electron scavengers, increasing the separation of photogenerated charges, while the crystalline defects introduced (Ti^{3+} and oxygen

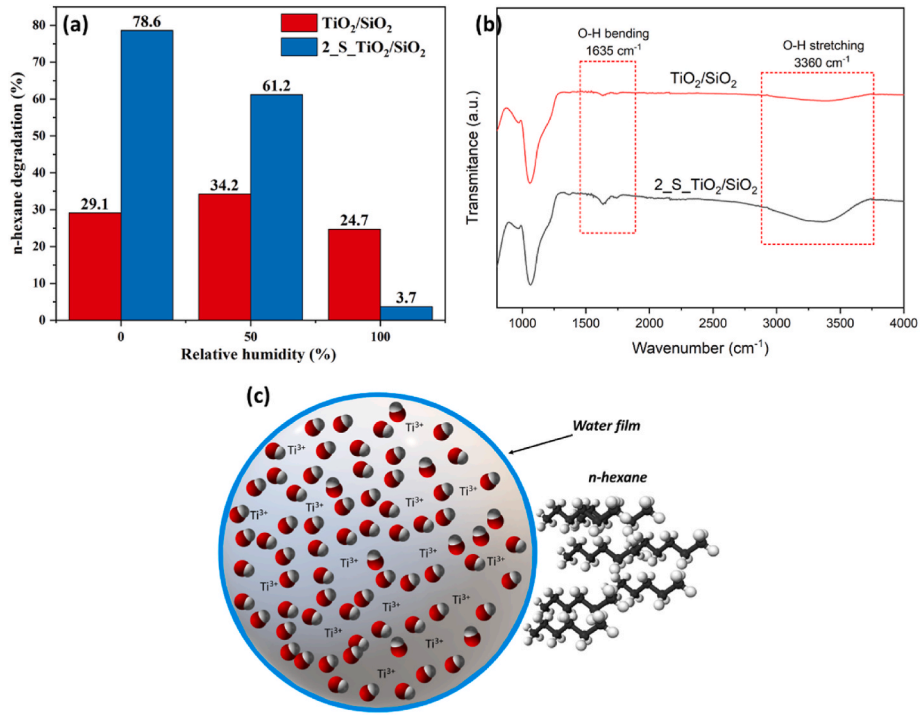

Fig. 8. (a) Evaluation of the effect of relative humidity for the TiO_2/SiO_2 and 2_S_TiO_2/SiO_2 materials; (b) Schematic representation of the blockage caused by water molecules adsorbed at 100 % of relative humidity for sample 2_S_TiO_2/SiO_2; (c) FTIR spectra of the dried TiO_2/SiO_2 and 2_S_TiO_2/SiO_2 samples.

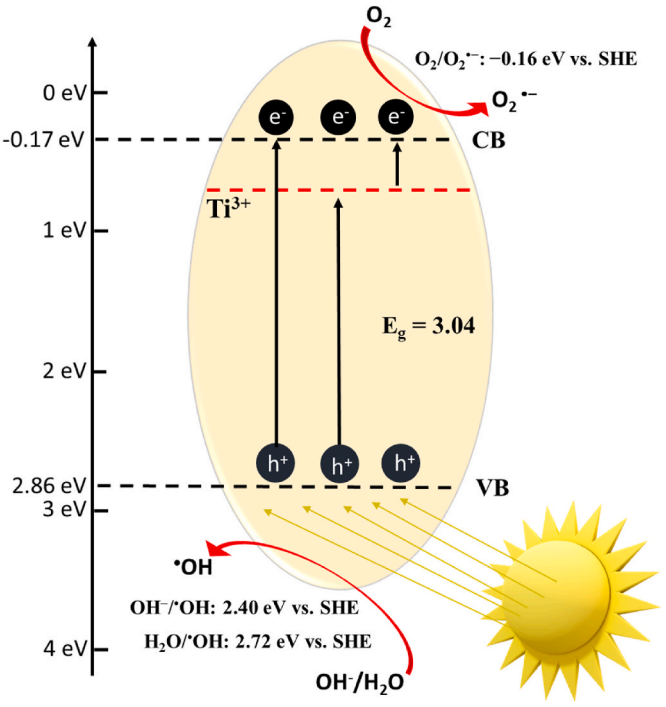

Fig. 9. Proposed photocatalytic mechanism for the 2_S_TiO_2/SiO_2 material.

vacancies) create energy mid-levels below the conduction band. This increases the population of electrons photoexcited into the conduction band, thereby increasing positive holes in the valence band. The experiments, with and without oxygen, highlight the significant role of the superoxide radical in *n*-hexane degradation. Notably, even at 0 % relative humidity, the gas stream exhibited the highest *n*-hexane degradation (78.6 %). Intriguingly, the FTIR spectra indicated persistent adsorbed water due to the oxygen vacancies, rendering the surface hyperhydrophilic.

Simultaneously, the persistence of a 14.6 % *n*-hexane degradation in the absence of oxygen suggests the involvement of hydroxyl radicals generated through the oxidation of OH^- and water adsorbed on the active sites, supporting their role in the reaction mechanism proposed in the conduction and valence band potential estimation. It is worth noting that, since the methodology for determining the valence and conduction band potentials relies on standard values of temperature and activity of the species involved and may differ from the actual conditions of the process, the experimental tests conducted evaluating the effect of oxygen and humidity were crucial to support the photocatalytic mechanism of the optimal material (2_S_TiO_2/SiO_2).

4. Conclusions

In this study, we used thiourea to introduce crystalline defects into TiO_2/SiO_2 using a simple and innovative method with varying mass ratios of sulfur to TiO_2. Subsequently, these materials were evaluated in a gas-solid photoreactor under UV–VIS light in the degradation of n-hexane. In light of the results obtained, we concluded that the incorporation of thiourea into the TiO_2/SiO_2 synthesis efficiently induced crystalline defects, the location and concentration of which were significantly impacted by the amount of sulfur precursor added. In addition, the fundamental role of relative humidity in gas-phase operation was highlighted, emphasizing the preference for carrying out reactions in a dry environment to obtain optimal photocatalytic behavior. In summary, this study provides valuable information on defect engineering and environmental considerations to increase the effectiveness of TiO_2/SiO_2 materials. It is important to emphasize that the performance of TiO_2/SiO_2 photocatalysts containing crystalline defects proposed in this work was evaluated using a light source with the same UV irradiance in the 300–400 nm wavelength range as the standard AM 1.5G solar spectrum at sea level. This ensures that the behavior of the modified material under natural sunlight conditions should be very similar to that obtained in our experiments, demonstrating the

applicability and viability of the materials developed for use in other photocatalytic processes.

Future work will focus on applying the optimized catalyst to degrade other volatile organic pollutants, especially those that are more recalcitrant, such as BTEX compounds. In addition, scaling up to a pilot-scale gas-phase fluidized photocatalytic reactor will be essential to evaluate the performance of the synthesized materials in larger-scale processes and confirm their practicality for industrial applications.

CRediT authorship contribution statement

Carolina Gusmão: Writing – original draft, Methodology, Investigation, Data curation, Conceptualization. **Priscila Hasse Palharim:** Writing – original draft, Software, Data curation. **Bruno Ramos:** Validation, Supervision, Software. **Douglas Gouvêa:** Writing – review & editing, Validation, Supervision. **Orlando Rodrigues Júnior:** Methodology, Investigation. **Antonio Carlos Silva Costa Teixeira:** Writing – review & editing, Validation, Supervision, Conceptualization.

Declaration of competing interest

The authors declare that they have no known competing financial interests or personal relationships that could have appeared to influence the work reported in this paper.

Acknowledgements

This study was financed in part by the Coordenação de Aperfeiçoamento de Pessoal de Nível Superior – Brasil (CAPES) – Finance Code 001. The authors also express their gratitude to the National Council of Scientific and Technological Development (CNPq, Brazil, grants #311230/2020-2 and #140347/2020-8), and to the São Paulo Research Foundation (FAPESP, grants PIPE #2016/00953-6, #2018/21271-6 and #2019/24158-9) for the financial support.

Appendix A. Supplementary data

Supplementary data to this article can be found online at https://doi.org/10.1016/j.ceramint.2025.03.172.

References

[1] E. David, V.-C. Niculescu, Volatile organic compounds (VOCs) as environmental pollutants: occurrence and mitigation using nanomaterials, Int. J. Environ. Res. Publ. Health 18 (2021) 13147, https://doi.org/10.3390/ijerph182413147.

[2] S. Almaie, V. Vatanpour, M.H. Rasoulifard, I. Koyuncu, Volatile organic compounds (VOCs) removal by photocatalysts: a review, Chemosphere 306 (2022) 135655, https://doi.org/10.1016/j.chemosphere.2022.135655.

[3] X. Li, L. Zhang, Z. Yang, P. Wang, Y. Yan, J. Ran, Adsorption materials for volatile organic compounds (VOCs) and the key factors for VOCs adsorption process: a review, Separ. Purif. Technol. 235 (2020) 116213, https://doi.org/10.1016/j.seppur.2019.116213.

[4] X. Liu, Y. Zhang, S. Matsushima, H. Hojo, H. Einaga, Photocatalytic oxidation process for treatment of gas phase benzene using Ti^{3+} self-doped TiO_2 microsphere with sea urchin-like structure, Chem. Eng. J. 402 (2020) 126220, https://doi.org/10.1016/j.cej.2020.126220.

[5] Y. Xu, S. Wu, P. Wan, J. Sun, Z.D. Hood, Introducing Ti^{3+} defects based on lattice distortion for enhanced visible light photoreactivity in TiO_2 microspheres, RSC Adv. 7 (2017) 32461–32467, https://doi.org/10.1039/C7RA04885H.

[6] Z. Li, S. Wang, J. Wu, W. Zhou, Recent progress in defective TiO_2 photocatalysts for energy and environmental applications, Renew. Sustain. Energy Rev. 156 (2022) 111980, https://doi.org/10.1016/j.rser.2021.111980.

[7] S. Chen, L. Zhang, L. Dai, W. Yu, J. Guan, S. Li, 3D monolithic composites TiO_2/HKUST-1/RGO@melamine foam with improved surface mass transfer for efficient photocatalytic degradation of toluene gas, Separ. Purif. Technol. 347 (2024) 127638, https://doi.org/10.1016/j.seppur.2024.127638.

[8] S. Chen, Y. Qi, C. Li, K. Domen, F. Zhang, Surface strategies for particulate photocatalysts toward artificial photosynthesis, Joule 2 (2018) 2260–2288, https://doi.org/10.1016/j.joule.2018.07.030.

[9] S. Liu, S. Yuan, Q. Zhang, B. Xu, C. Wang, M. Zhang, T. Ohno, Fabrication and characterization of black TiO_2 with different Ti^{3+} concentrations under atmospheric conditions, J. Catal. 366 (2018) 282–288, https://doi.org/10.1016/j.jcat.2018.07.018.

[10] Z. Xiu, M. Guo, T. Zhao, K. Pan, Z. Xing, Z. Li, W. Zhou, Recent advances in Ti^{3+} self-doped nanostructured TiO_2 visible light photocatalysts for environmental and energy applications, Chem. Eng. J. 382 (2020) 123011, https://doi.org/10.1016/j.cej.2019.123011.

[11] Z. Pei, S. Weng, P. Liu, Enhanced photocatalytic activity by bulk trapping and spatial separation of charge carriers: a case study of defect and facet mediated TiO_2, Appl. Catal. B Environ. 180 (2016) 463–470, https://doi.org/10.1016/j.apcatb.2015.06.045.

[12] Q. Zhu, Y. Peng, L. Lin, C.-M. Fan, G.-Q. Gao, R.-X. Wang, A.-W. Xu, Stable blue TiO_2−x nanoparticles for efficient visible light photocatalysts, J. Mater. Chem. A 2 (2014) 4429–4437, https://doi.org/10.1039/C3TA14484D.

[13] Y. Chen, X. Fu, Z. Peng, A Review on oxygen-deficient titanium oxide for photocatalytic hydrogen production, Metals 13 (2023) 1163, https://doi.org/10.3390/met13071163.

[14] Y. Chen, K. Wang, L. Lou, Photodegradation of dye pollutants on silica gel supported TiO_2 particles under visible light irradiation, J. Photochem. Photobiol. Chem. 163 (2004) 281–287, https://doi.org/10.1016/j.jphotochem.2003.12.012.

[15] C. de A. Gusmão, P.H. Palharim, B. Ramos, A.C.S.C. Teixeira, Enhancing the visible-light photoactivity of silica-supported TiO_2 for the photocatalytic treatment of pharmaceuticals in water, Environ. Sci. Pollut. Control Ser. 29 (2022) 42215–42230, https://doi.org/10.1007/s11356-021-16718-w.

[16] C. de A. Gusmão, L.A. Diniz, B. Ramos, A.G. Câmara, J.G.A. Pacheco, A.C.S. C. Teixeira, Optimization of TiO_2/SiO_2 photocatalysts in a LED-irradiated gas-solid photoreactor for air treatment, Chem. Eng. Res. Des. 185 (2022) 223–238, https://doi.org/10.1016/j.cherd.2022.07.001.

[17] C. de A. Gusmão, L.T. Borges, P.H. Palharim, L. Otubo, O. Rodrigues, D. Gouvea, B. Ramos, A.C.S.C. Teixeira, Synthesis, characterization, and application of Pt/PtO_2-TiO_2/SiO_2 materials on a continuous flow packed bed microreactor for enhanced photocatalytic activity under sunlight, Water 14 (2022) 3864, https://doi.org/10.3390/w14233864.

[18] B. Bharti, H. Li, D. Liu, H. Kumar, V. Manikandan, X. Zha, F. Ouyang, Efficient Zr-doped FS–TiO_2/SiO_2 photocatalyst and its performance in acrylonitrile removal under simulated sunlight, Appl. Phys. A 126 (2020) 887, https://doi.org/10.1007/s00339-020-04066-4.

[19] O. Carp, C.L. Huisman, A. Reller, Photoinduced reactivity of titanium dioxide, Prog. Solid State Chem. 32 (2004) 33–177, https://doi.org/10.1016/j.progsolidstchem.2004.08.001.

[20] A.A. Bernardes, A.L. da Silva, B. Ramos, F.C. Fonseca, D. Gouvêa, Intrinsic defects generated by iodine during TiO_2 crystallization and its relationship with electrical conductivity and photoactivity, International Journal of Ceramic Engineering & Science 5 (2023) e10186, https://doi.org/10.1002/ces2.10186.

[21] S. Sahu, P. Rani Sahoo, S. Patel, B.K. Mishra, Oxidation of thiourea and substituted thioureas: a review, J. Sulfur Chem. 32 (2011) 171–197, https://doi.org/10.1080/17415993.2010.550294.

[22] R. Shi, Y. Chen, Controlled Formation of defective shell on TiO_2 (001) facets for enhanced photocatalytic CO_2 reduction, ChemCatChem 11 (2019) 2270–2276, https://doi.org/10.1002/cctc.201900061.

[23] R.V. Nair, V.S. Gummaluri, M.V. Matham, V. C, A review on optical bandgap engineering in TiO_2 nanostructures via doping and intrinsic vacancy modulation towards visible light applications, J. Phys. Appl. Phys. 55 (2022) 313003, https://doi.org/10.1088/1361-6463/ac6135.

[24] T.S. Rajaraman, S.P. Parikh, V.G. Gandhi, Black TiO_2: a review of its properties and conflicting trends, Chem. Eng. J. 389 (2020) 123918, https://doi.org/10.1016/j.cej.2019.123918.

[25] J. Yan, G. Wu, N. Guan, L. Li, Z. Li, X. Cao, Understanding the effect of surface/bulk defects on the photocatalytic activity of TiO_2: anatase versus rutile, Phys. Chem. Chem. Phys. 15 (2013) 10978–10988, https://doi.org/10.1039/C3CP50927C.

[26] M. Kong, Y. Li, X. Chen, T. Tian, P. Fang, F. Zheng, X. Zhao, Tuning the relative concentration ratio of bulk defects to surface defects in tio_2 nanocrystals leads to high photocatalytic efficiency, J. Am. Chem. Soc. 133 (2011) 16414–16417, https://doi.org/10.1021/ja207826q.

[27] X. Yu, B. Kim, Y.K. Kim, Highly Enhanced photoactivity of anatase TiO_2 nanocrystals by controlled hydrogenation-induced surface defects, ACS Catal. 3 (2013) 2479–2486, https://doi.org/10.1021/cs4005776.

[28] X. Xin, T. Xu, J. Yin, L. Wang, C. Wang, Management on the location and concentration of Ti^{3+} in anatase TiO_2 for defects-induced visible-light photocatalysis, Appl. Catal. B Environ. 176–177 (2015) 354–362, https://doi.org/10.1016/j.apcatb.2015.04.016.

[29] X. Liu, B. Hou, G. Wang, Z. Cui, X. Zhu, X. Wang, Black titania/graphene oxide nanocomposite films with excellent photothermal property for solar steam generation, J. Mater. Res. 33 (2018) 674–684, https://doi.org/10.1557/jmr.2018.25.

[30] M.M. Khan, S.A. Ansari, D. Pradhan, M.O. Ansari, D.H. Han, J. Lee, M.H. Cho, Band gap engineered TiO_2 nanoparticles for visible light induced photoelectrochemical and photocatalytic studies, J. Mater. Chem. A 2 (2013) 637–644, https://doi.org/10.1039/C3TA14052K.

[31] W. Kongsuebchart, P. Praserthdam, J. Panpranot, A. Sirisuk, P. Supphasrirongjaroen, C. Satayaprasert, Effect of crystallite size on the surface defect of nano-TiO_2 prepared via solvothermal synthesis, J. Cryst. Growth 297 (2006) 234–238, https://doi.org/10.1016/j.jcrysgro.2006.09.018.

[32] Z. Wu, Z. Sheng, Y. Liu, H. Wang, N. Tang, J. Wang, Characterization and activity of Pd-modified TiO_2 catalysts for photocatalytic oxidation of NO in gas phase, J. Hazard Mater. 164 (2009) 542–548, https://doi.org/10.1016/j.jhazmat.2008.08.028.

[33] Y. Wu, Y. Fu, L. Zhang, Y. Ren, X. Chen, B. Yue, H. He, Study of oxygen vacancies on different facets of anatase TiO_2, Chin. J. Chem. 37 (2019) 922–928, https://doi.org/10.1002/cjoc.201900188.
[34] M. O'Loughlin, C. Priest, M.N. Popescu, J. Ralston, Patterning of wettability for controlling capillary-driven flow in closed channels, J. Colloid Interface Sci. 402 (2013) 259–266, https://doi.org/10.1016/j.jcis.2013.03.058.
[35] J. Saari, H. Ali-Löytty, M.M. Kauppinen, M. Hannula, R. Khan, K. Lahtonen, L. Palmolahti, A. Tukiainen, H. Grönbeck, N.V. Tkachenko, M. Valden, Tunable Ti^{3+}-mediated charge carrier dynamics of atomic layer deposition-grown amorphous TiO_2, J. Phys. Chem. C 126 (2022) 4542–4554, https://doi.org/10.1021/acs.jpcc.1c10919.
[36] P.H. Palharim, M. Clara D'Amaro Caira, C. Gusmão, B. Ramos, A. Gomes da Câmara, J.G.A. Pacheco, O. Rodrigues, A.C.S.C. Teixeira, Enhanced photocatalytic activity and stability of WO_3-AgCl/Ag composites: surface modulation by structure-directing agents for effective sunlight treatment of pharmaceutical wastewater, J. Photochem. Photobiol. Chem. (2023) 115433, https://doi.org/10.1016/j.jphotochem.2023.115433.
[37] R.A. Senthil, S. Osman, J. Pan, M. Sun, A. Khan, V. Yang, Y. Sun, A facile single-pot synthesis of WO_3/AgCl composite with enhanced photocatalytic and photoelectrochemical performance under visible-light irradiation, Colloids Surf. A Physicochem. Eng. Asp. 567 (2019) 171–183, https://doi.org/10.1016/j.colsurfa.2019.01.056.
[38] H.S. Mahal, S. Kapoor, A.K. Satpati, T. Mukherjee, Radical Scavenging and catalytic activity of metal−phenolic complexes, J. Phys. Chem. B 109 (2005) 24197–24202, https://doi.org/10.1021/jp0549430.
[39] P.H. Palharim, B.L.D.R. Fusari, B. Ramos, L. Otubo, A.C.S.C. Teixeira, Effect of HCl and HNO_3 on the synthesis of pure and silver-based WO_3 for improved photocatalytic activity under sunlight, J. Photochem. Photobiol. Chem. 422 (2022) 113550, https://doi.org/10.1016/j.jphotochem.2021.113550.
[40] N. Belkessa, A. Bouzana, A.A. Assadi, Understanding of the synergy effect of DBD plasma discharge combined to photocatalysis in the case of Ethylbenzene removal: interaction between plasma reactive species and catalyst, J. Environ. Chem. Eng. 11 (2023) 110640, https://doi.org/10.1016/j.jece.2023.110640.
[41] U.L. Rochetto, E. Tomaz, Degradation of volatile organic compounds in the gas phase by heterogeneous photocatalysis with titanium dioxide/ultraviolet light, J. Air Waste Manag. Assoc. 65 (2015) 810–817, https://doi.org/10.1080/10962247.2015.1020117.
[42] A. Maudhuit, C. Raillard, V. Héquet, L. Le Coq, J. Sablayrolles, L. Molins, Adsorption phenomena in photocatalytic reactions: the case of toluene, acetone and heptane, Chem. Eng. J. 170 (2011) 464–470, https://doi.org/10.1016/j.cej.2011.02.040.
[43] D. Matsumoto, L.A. Diniz, L.S. Castro, A.C.S.C. Teixeira, R. Guardani, J.L. de Paiva, Kinetic modeling and experimental validation of a photocatalytic fluidized bed reactor for n-hexane degradation, Braz. J. Chem. Eng. 36 (2019) 1561–1570, https://doi.org/10.1590/0104-6632.20190364s20180558.
[44] F. Moulis, J. Krýsa, Photocatalytic degradation of several VOCs (n-hexane, n-butyl acetate and toluene) on TiO_2 layer in a closed-loop reactor, Catal. Today 209 (2013) 153–158, https://doi.org/10.1016/j.cattod.2012.10.017.
[45] J.O. Saucedo-Lucero, S. Arriaga, Photocatalytic degradation of hexane vapors in batch and continuous systems using impregnated ZnO nanoparticles, Chem. Eng. J. 218 (2013) 358–367, https://doi.org/10.1016/j.cej.2012.12.050.
[46] A.K. Boulamanti, C.J. Philippopoulos, Photocatalytic degradation of C5–C7 alkanes in the gas–phase, Atmos. Environ. 43 (2009) 3168–3174, https://doi.org/10.1016/j.atmosenv.2009.03.036.
[47] T. Watanabe, N. Yoshida, Wettability control of a solid surface by utilizing photocatalysis, Chem. Rec. 8 (2008) 279–290, https://doi.org/10.1002/tcr.20154.
[48] Z. Gao, H. Yang, J. Mao, L. Kang, R. Zhang, S. Chai, J. Wu, W. Li, Araneose Ti^{3+} self-doping TiO_2/SiO_2 nanowires membrane for removal of aqueous MB under visible light irradiation, Environ. Sci. Pollut. Control Ser. 27 (2020) 9748–9759, https://doi.org/10.1007/s11356-019-07567-9.